Damage identification using modal strains identified from operational fiber-optic Bragg grating data ☆,☆☆

Dimitrios Anastasopoulos[a,*], Maure De Smedt[b], Lucie Vandewalle[b], Guido De Roeck[a], Edwin P.B. Reynders[a]

[a] *Structural Mechanics Section, Dept. of Civil Engineering, University of Leuven (KU Leuven), Leuven, Belgium*
[b] *Building Materials and Building Technology Section, Dept. of Civil Engineering, University of Leuven (KU Leuven), Leuven, Belgium*

Abstract

Vibration-based structural health monitoring of civil structures relies on the repeated identification of dynamic structural characteristics of the structure from output-only vibration data. Natural frequencies and displacement mode shapes are the most commonly employed dynamic characteristics, yet their sensitivity to local damage of moderate severity is rather low with respect to their sensitivity to other factors such as temperature, necessitating data normalization. Strain mode shapes offer a higher sensitivity to local damage, but their accurate identification in a dense grid is challenging given the very small dynamic strain levels that are encountered under ambient excitation. In this paper, a method is presented for tackling this challenge. It consists of three stages. Firstly, fiber optic Bragg grating strain sensors are attached to the structure and interrogated with a tunable laser performing a wavelength sweep. In this way, the measured strain amplitudes have the required accuracy but synchronization errors are introduced between the different Bragg sensors. Secondly, a modal analysis is performed on the dynamic strain data using an accurate parametric system identification technique. This is followed by a synchronization step which compensates for the delays introduced by the wavelength sweep. Finally, the synchronized strain mode shapes are employed as damage-sensitive features, either directly or via a newly proposed quantity, the top-to-bottom strain ratio. The method is validated by progressive damage testing of a complex, prestressed concrete "roof" beam, reinforced with steel fibers. It is observed that the proposed method can identify both the presence and the location of the damage in a relatively early stage.

Keywords: Structural health monitoring, damage identification, strain mode shapes, experimental modal analysis, fiber-optic sensors

☆ *Postprint submitted to Structural Health Monitoring*

☆☆ *Published version:* D. Anastasopoulos, M. De Smedt, L. Vandewalle, G. De Roeck, and E. P.B. Reynders. Damage identification using modal strains identified from operational fiber-optic Bragg grating data. *Structural Health Monitoring*, 00:00–00, 2018. https://doi.org/10.1177/1475921717744480

*Corresponding author. Tel.: +32 (0) 16 37 45 69.
Email address: dimitrios.anastasopoulos@kuleuven.be (Dimitrios Anastasopoulos)

1. Introduction

As many civil structures, such as bridges, dams and tunnels are approaching or even exceeding their original design life, the development of reliable structural health monitoring (SHM) techniques that provide information about the structure's condition becomes necessary. This information can be elaborated in a decision supporting system, e.g. whether or not to extend the operation of a structure beyond its original design service life, offering multiple safety and economic benefits [1]. SHM systems can be introduced to structures at any phase of their service life and their structural condition at the moment of the implementation of the SHM system is then considered as the baseline condition. Damage can then be identified by comparing future observations with the baseline observations. Thus, an early-installed SHM system increases the chances of damage identification at any moment of the structure's service life; for this reason, SHM systems are also deployed right after construction [1, 2].

Vibration-based structural health monitoring, usually abbreviated as VBSHM or VBM, is a non-destructive condition assessment method, based on the identification of changes in the dynamic characteristics of a structure, which are directly related to damage [3]. The main challenge for VBSHM is to identify dynamic characteristics that are as sensitive as possible to structural damage and at the same time as insensitive as possible to measurement noise, loading, and environmental factors such as temperature. Dynamic characteristics which are used very often in VBSHM are the natural frequencies. However, natural frequencies are influenced by environmental factors, such as temperature, and that influence can be high enough to completely mask the presence of even severe damage, necessitating data normalization [4, 5, 6, 7, 8, 9, 10]. Furthermore, natural frequencies are global structural characteristics and therefore they can not assess the location of damage while their sensitivity to certain types of damage can be low [5]. A promising alternative can be the monitoring of dynamic characteristics obtained from dynamic strain measurements, such as modal strains and modal curvatures which are more sensitive to local damage than modal displacements, offering in this way a higher accuracy in damage detection and localization [11, 12, 13, 14]. The same studies point out also the importance of obtaining the modal curvatures directly from measured axial modal strains rather than by using numerical differentiation of measured vertical modal displacements since such differentiation is known to be numerically ill-conditioned. Additionally, it can be hard to obtain modal displacements and consequently modal curvatures from accelerometer measurements for frequencies below 1 Hz, in contrary with the strain sensors that can practically be used from 0 Hz (static measurements). However, the accurate determination of the modal strains is challenging given the very small (sub-microstrain) dynamic strain levels that are encountered in civil structures under ambient excitation. Ease of implementation and cost-effectiveness are important additional concerns [3].

The introduction of fiber-optic sensor (FOS) systems opened up new possibilities for strain-based SHM in general, and VBSHM in particular [15]. In the past years, fiber-optic sensors such as interferometric FOS [16] that are based on the principle of low-coherence interferometry, have been successfully used in operational modal analysis for SHM [12, 17, 18]. High accuracy in dynamic strain measurements has been achieved with interferometric FOS [12]. However, interferometric FOS do not offer the benefit of measuring in a dense grid, since a limited amount of sensors can be continuously monitored from a single acquisition unit while their multiplexing capability is also limited [16]. Fiber Bragg Grating (FBG) sensors [19] share important advantages with other fiber optic sensors, such as electro-magnetic immunity, long-term stability, and resistance in harsh environments, but additionally they are easy to multiplex (i.e., many different sensors with different

operating wavelengths can be inscribed into the same glass fiber) and they have a relatively low cost [20]. Thanks to the multiplexing option, structures can be monitored with a large number of sensors and in a dense grid. FBGs are being used for real-time monitoring of railway infrastructure [21], wind turbines [22] and bridges [23]. The Tsing Ma Bridge in Hong Kong is an example of a structure on which FBGs are used for SHM purposes. There, the dynamic strains that are imposed on the bridge by the traffic are measured with a limited number of sensors; the corresponding strain amplitudes though are much larger than on most other structures (tens of microstrains) [24].

However, measuring the very small dynamic strains that occur in civil structures during ambient or operational excitation with high accuracy and precision and in a dense grid remains a very important challenge. One recently proposed approach consists of replacing the standard wavelength shift detection algorithm in a commercial broadband FBG interrogator with a more advanced optical signal processing algorithm, such that sub-microstrain accuracy can be achieved with FBG sensing [25]. In this paper, an alternative FBG-based method is presented, the advantage of which is that it is non-intrusive, i.e., it does not interfere with the FBG interrogator. Instead of employing an FBG interrogator with a broadband light source, an interrogator with a tunable laser source is employed (throughout this paper, it is referred to as the FBGS FAZT-I4 interrogator). The tunable laser source scans each FBG sensor individually with a wavelength sweep. This offers a high wavelength resolution and therefore a high accuracy of the measured strain amplitudes. However, the sweep also introduces delays between the different FBG sensors. These delays are not compensated for in the first instance, instead a modal analysis is performed directly on the acquired data using an accurate parametric system identification technique. The strain mode shapes that are obtained in this way are complex due to the time delays introduced during the acquisition, and this complexity is then exploited for synchronization with a novel technique, the accuracy of which was already investigated in a different context [26]. Subsequently, potential damage is identified by repetitively identifying strain mode shapes and monitoring the changes over time. Next to a direct comparison of the strain mode shapes, the top-to-bottom strain ratio is also introduced as a damage-sensitive feature.

The method is presented through application in a progressive damage test (PDT) on a complex, prestressed fiber-reinforced concrete "roof" beam. The beam is monitored with three chains of multiplexed FBG sensors and conventional uniaxial accelerometers. It is excited with an impulse hammer at low force amplitudes, resulting in dynamic strains of sub-microstrain amplitude. Dynamic tests are performed at the end of each loading cycle and the data are used in two modal analyses; an acceleration-based modal analysis and a strain-based modal analysis. The obtained dynamic characteristics of the various damage stages are then compared and shifts in their values are related to the presence and location of structural damage.

The paper is organized as follows. Firstly, the experimental setups that are used for the quasi-static progressive damage test and the intermediate dynamic tests are described. Secondly, in order to get more insight into the structural behavior of the "roof" beam, a finite element model (FEM) is constructed and employed for estimating the detailed modal characteristics of the "roof beam in undamaged condition. Thirdly, the dynamic characteristics for the various loading cycles that are obtained with the novel approach outlined above are presented, and extensive comparisons for damage identification and localization are performed.

Figure 1: The experimental setup of the modal test and the PDT.

2. Experimental setup

A prestressed concrete beam of I-shaped cross-section, with a variable height (i.e. roof-shaped) and openings in the web serves as the test structure (Figure 1). The length of the beam is 6.0 m and the height varies linearly from 0.75 m at its ends to 0.90 m in the middle. The flange width equals 0.29 m whereas the web width equals 0.08 m. 7-wire low relaxation strands with a nominal diameter of 12.5 mm are used for prestressing: seven at the bottom and one at the top of the beam. The strands are given an initial prestrain of $7.5 \cdot 10^{-3}$ mm/mm (σ_{p0} equal to 1488 MPa). Splitting reinforcement, with a nominal diameter of 8 mm and a centre-to-centre distance of 50 mm, is provided to withstand the gradual growth of the prestressing force over the beam's height. In addition, each side of the web openings is reinforced with two rebars of diameter 8 mm.

The mean cube compressive strength $f_{cm,cube}$, measured according to EN 12390-3 [27], equals 97.3 MPa. The concrete is supplemented with 40 kg/m^3 of steel fibres (DRAMIX RC-80/30-CP; length of 30 mm, diameter of 0.38 mm, and tensile strength of 3070 MPa). For this steel fibre reinforced concrete, the crack mouth opening displacement-stress (CMOD-σ) curve is measured according to EN 14561 [28]. As presented in Figure 2, using 40 kg/m^3 of steel fibres results in a hardening behaviour under bending and the mean flexural tensile strength $f_{ctm,fl}$ equals 5.4 MPa. Furthermore, the material properties, i.e. static Young's modulus E_{cm} and density ρ_m, which will be assigned in the finite element model, have been measured according to EN 12390-13 [29] and EN 12390-1 [30] respectively. Their values are $E_{cm} = 46$ GPa and $\rho_m = 2350$ kg/m^3 (Table 1).

2.1. Progressive damage test

The beam is subjected to a three-point bending, progressive damage test, which is carried out in load control using a hydraulic press (Instron, capacity 2.5 MN). The quasi-static load is applied at the middle of the beam while the beam is supported on a steel table through two supports at 1.0 m from the ends (Figures 3 and 4). The static boundary conditions approximate these of a simply supported beam. However, this is not the case for the dynamic behavior: a complex dynamic interaction between the beam and the steel table is expected as the steel table cannot be considered as infinitely stiff with respect to the concrete beam.

A progressive damage loading scheme until failure is followed, consisting of eleven loading cycles of increasing load, where the load step was 50 kN and the (un)loading rate 1 kN/s. Besides the force and displacement measurement of the hydraulic press head, linear variable differential transformers (LVDTs) and a photoelectric sensor (Baumer Photoelectric OADM 12U6460 with

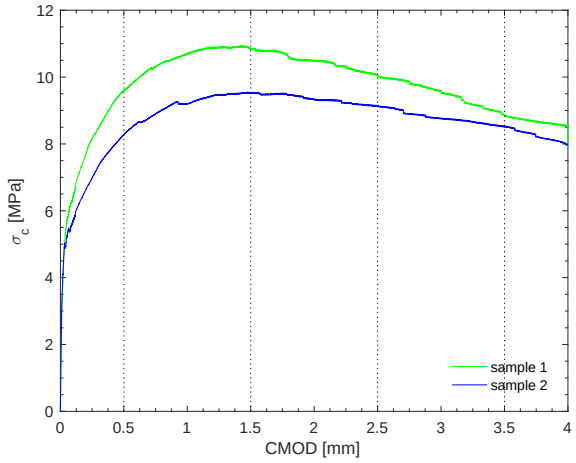

Figure 2: Experimentally obtained CMOD-σ curve for the concrete mixture with 40 kg/m^3 of steel fibres.

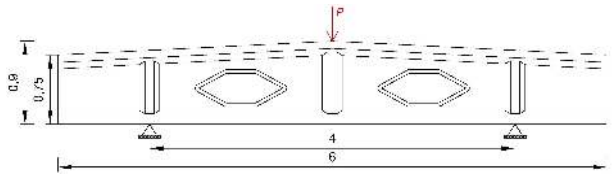

Figure 3: The three-point PDT. The quasi-static force P is applied in the direction of the arrow. (Dimensions in meter)

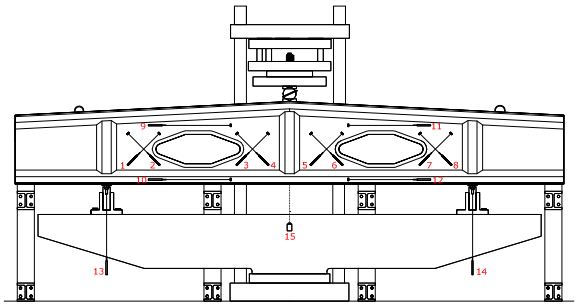

Figure 4: Location of the 12 LVDTs in the shear zone, the 2 LVDTs at the supporting points (number 13 and 14) and the optical sensor (number 15).

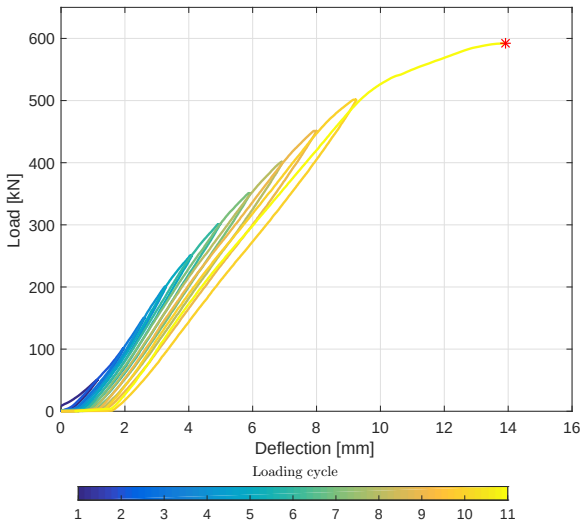

Figure 5: The load-displacement curve of the PDT.

resolution $96 \cdot 10^{-3}$ mm) are used to measure displacements. The photoelectric sensor measures the deflection at midspan of the beam and two LVDTs measure the displacements of the supporting points. Twelve LVDTs are used to measure the deformation of the beam in the shear zones, as illustrated in Figure 4.

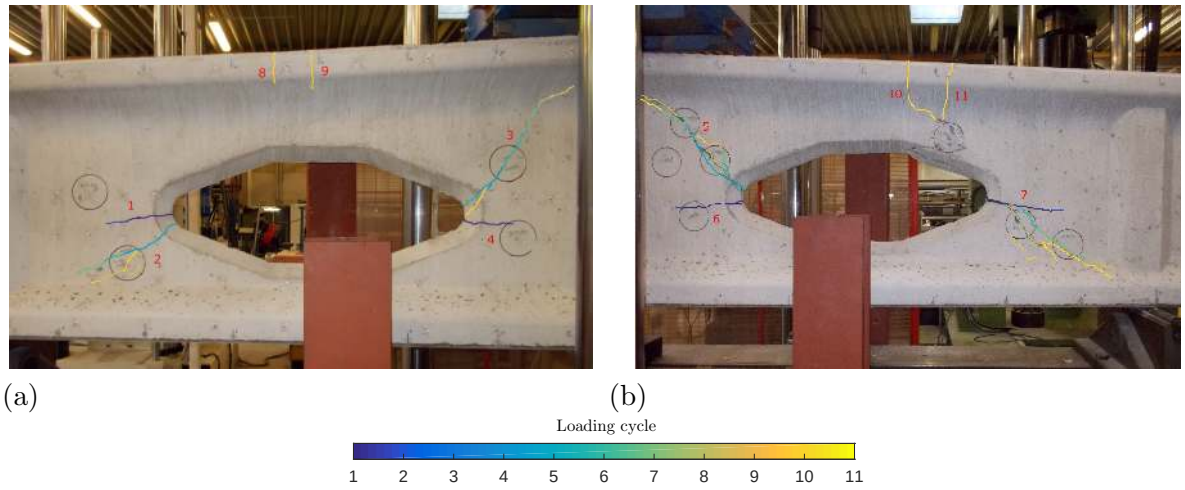

Figure 6: Evolution of the the main shear cracks for the 11 loading cycles. (a) Cracks 1-4 and 8-9, (b) Cracks 5-7 and 10-11.

Figure 5 shows the measured load-displacement curve of the quasi-static loading cycles. The beam failed in shear during the eleventh loading cycle at a load of 592 kN. As expected, the failure cracks occurred in the shear span between loading and supporting points, although some bending cracks at the middle were detectable as well. At the beginning of testing, small concrete hardening cracks around the web openings and at the top of the beam were observable, which were also aggravated from the prestressing force. These cracks extended during the second loading cycle up

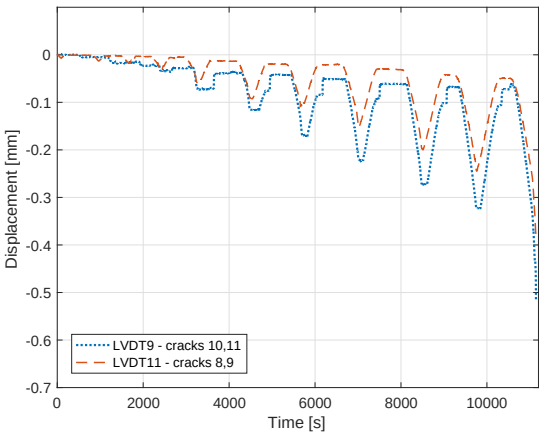

Figure 7: The quasi-static deformation history of the LVDTs in compression above the web openings during the 11 loading cycles.

to 100 kN. The first shear cracks were observed during the fifth loading cycle at 250 kN. Each subsequent loading cycle enlarged the shear cracks until the shear failure in the eleventh loading cycle. Besides, due to the enlarging shear cracks, the height of the compression zone decreased and crushing of the concrete occurred at the top of the beam.

Figure 6 presents the pattern of the shear failure and the main cracks at both sides of the beam. The largest deformations were measured by the LVDTs crossing these cracks, namely LVDTs 2, 4, 5 and 7. Figure 7 displays the shortening at the top of the web openings during the eleven loading cycles, measured by LVDTs 9 and 11 (cracks 8-11 in Figure 6). The eleven loading cycles of these LVDTs are shown in Figure 8 and the measured deformations correspond to pure cracks width since the shear deformation is considered to be negligible. In Figure 9, the maximum crack widths with respect to the maximum loads at each loading cycle are plotted. Although the largest deformations occur at the side of cracks 1-4, the beam finally failed in shear at the other side, along cracks 5, 7, 10 and 11 because of the redistribution of forces due to the reduction of local stiffness.

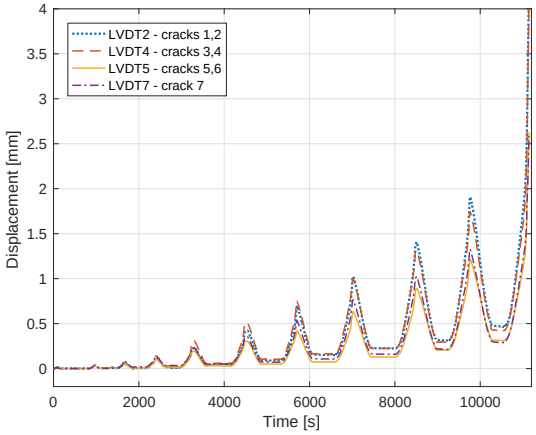

Figure 8: The quasi-static deformation history of the LVDTs in tension crossing the shear cracks during the 11 loading cycles.

The presence of the large holes in the “roof” beam complicates its structural behavior. This is

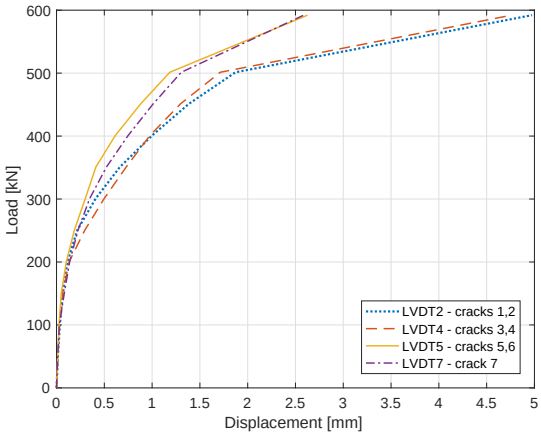

Figure 9: The maximum deformation (crack width) per loading cycle of the LVDTs crossing the shear cracks.

also observed from the crack pattern. For regular solid beams, large bending cracks would occur either at the bottom or at the top of the beam (depending on the loading), i.e., close to where the longitudinal dynamic strains are measured (see further). However, in the present case most cracks occur around the openings and away from the dynamic strain sensors, which makes this case more challenging for SHM.

2.2. Dynamic tests

The dynamic excitation of the beam is performed with impulse hammer impacts in the vertical (z-axis in Figures 10-14) and the lateral (y-axis, out of plane in Figures 10-14) direction. Two tests are conducted after the end of each loading cycle, when the applied quasi-static load is zero and the head of the hydraulic press detached. For the first test, the beam is excited in the vertical direction with 50 hammer impacts (continuous measurement) at location 1 (Figure 10). For the second test, the same procedure is followed but the lateral direction is excited with 50 hammer impacts at location 2L (Figure 12). Hence, data from 22 tests (2 per loading cycle) are available. The response of the beam to the induced dynamic excitation is recorded with uniaxial accelerometers from PCB Piezotronics and Dytran Instruments, and FBG strain sensors from FBGS.

The vertical response of the beam is monitored with 23 accelerometers that are attached to the top (Figures 10 and 11). Furthermore, 8 accelerometers are attached to the side of the beam to measure its lateral response. Two acquisition systems are used, due to the large number of channels that are required for measuring both the vertical and the lateral accelerometers. A National Instruments (NI) PXI-1050 chassis acquisition system is used for the vertical accelerometers (1-23 in Figure 10). The sampling frequency is $f_{s,v} = 1000$ Hz. A National Instruments (NI) cDAQ-9178 compact acquisition system is used for the lateral accelerometers (1L-8L in Figure 12). The sampling frequency is $f_{s,l} = 1651$ Hz. The difference in the sampling frequency is due to the fact that the cDAQ-9178 has a fixed sampling frequency. The sampling frequency for the vertical accelerometers is selected to be equal with the maximum sampling frequency of the strain acquisition system.

The dynamic strains of the beam are measured with three chains of multiplexed FBG strain sensors; two at the top flange and one at the bottom flange (Figures 13-14) of the beam. The chains are attached to the side of the top and the bottom flange of the beam along its longitudinal direction through a custom clamping system, to measure axial dynamic strains. The connections

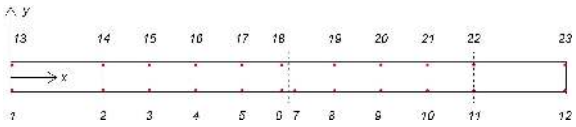

Figure 10: The vertical accelerometers setup - Top view.

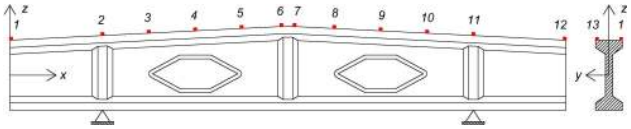

Figure 11: The vertical accelerometers setup - Front view and cross section.

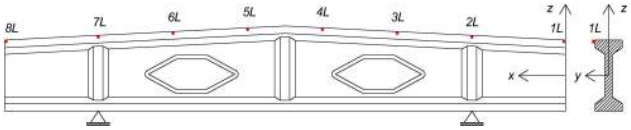

Figure 12: The lateral accelerometers setup - Front view and cross section.

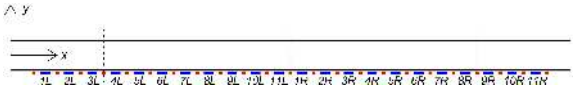

Figure 13: The FBG setup - Top view.

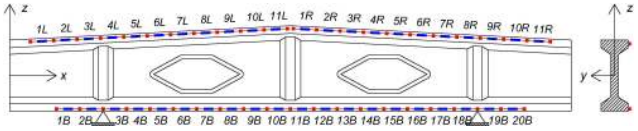

Figure 14: The FBG setup - Front view and cross section.

of the clamping system are directly glued on the beam. They consist of two parts, the base and the cap, as shown is Figures 15-16. The fiber is fixed between the two parts, by firmly screwing the cap to the base, so that it can not slide and the strains can adequately be transferred from the beam to the sensors. Rubber is used in the connection to ensure that the fiber will not get damaged.

The two chains of FBG sensors that are attached to the top flange contain in total 22 sensors (11 per chain). The bottom chain contains 20 FBG sensors (Figure 14). The fibers are firmly fixed at the discrete connections (Figure 15) to ensure the proper transfer of strains from the beam to the sensors. The distance between two consecutive connections is 25 cm and one FBG sensor exists between them, measuring the average strain or macro-strain between both connections. Since the FBGs are multiplexed onto the same fiber, the macro-strains are measured in a quasi-distributed way along the length of the beam, enabling a clear physical interpretation. On the contrary, if the FBG sensors would be directly glued onto the beam, they would measure only very local strains, the precise interpretation of which is much harder, as they highly depend on the precise position of the FBG sensors with respect to the cracks. The fibers are prestressed to ensure that they would remain in tension due to the applied quasi-static force during the PDT. Thermal insulation is also provided around the fibers to ensure that temperature fluctuations in the laboratory would not

Figure 15: A typical connection of the clamping system.

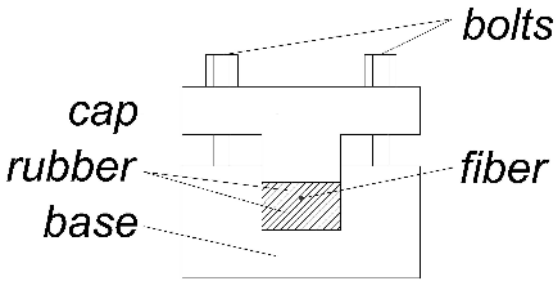

Figure 16: Detail of a typical connection of the clamping system.

affect the measurements (Figures 1 and 15). The progressive damage test is conducted indoors under controlled temperature conditions and in a time period that spanned less than three hours. Therefore, it is considered that only small temperature fluctuations ($\pm 1^{\circ}C$) can occur during the experiment that are not able to influence the dynamic characteristics of the beam in the short period of time that the experiment lasts. Consequently the influence of the temperature on the dynamic characteristics is considered negligible.

When dynamic strains are measured, the ability to determine the Bragg wavelength shift with adequate accuracy and precision is essential. Therefore, the strain acquisition system is an interrogator of relatively high wavelength accuracy (± 1 pm) and precision (< 0.1 pm), the FBGS FAZT-I4. The accuracy is defined as the proximity of the measurements to the actual values while the precision is defined as the degree to which repeated measurements under unchanged conditions show the same results [31]. The FAZT-I4 has four channels that are simultaneously scanned by a tunable laser source, offering the simultaneous interrogating of four FBG fibers with a maximum of 30 FBGs per fiber. When the measured wavelength shifts are lower than the resolution of the acquisition system, the implementation of a method that will interpolate the wavelength spectrum down to the desired resolution level is mandatory [25]. However, the resolution of the I4 is adequate for the presented work, and therefore no method needs to be implemented. The position-averaged root mean square (RMS) strain value of the dynamic strain measurements is about 0.3 $\mu\epsilon$. The sampling frequency is $f_{s,s} = 1000$ Hz.

3. Dynamic finite element model

A three-dimensional (solid) linear elastic finite element model (FEM) of the undamaged beam is built in ANSYS 15.0 in order to predict the dynamic characteristics of the undamaged beam. The element type SOLID 187 is selected from the ANSYS element library which allows to model

straightforwardly the whole beam. SOLID 187 is a higher order, 10-node element with 3 displacement degrees of freedom per node and a quadratic displacement shape function. The element is well suited for irregular meshes [32]. The finite element mesh that is employed in the modal analysis is chosen based on the following criteria: (a) the geometry of the structure would be captured as accurately as possible, (b) the finite element shapes would not be over-distorted and (c) the computed natural frequencies of interest would change $\ll 1\%$ with additional mesh refinement. Based on these criteria, the chosen finite element mesh size is about 10 cm, which provides the necessary accuracy for the objectives of this research.

Dynamic free-free boundary conditions are applied in the FEM, which do not fully correspond to the actual dynamic boundary conditions of the beam. The FEM does not take into account the strong vertical interaction of the beam with the supporting beam that influences many of its modes. Since in the test setup the lateral displacement of the beam is restrained only by the friction at the supports, the beam is allowed to move freely also in the lateral direction in the FEM. Eleven vertical, lateral, and torsion modes are calculated in the frequency range [0-350] Hz. The obtained natural frequency values and displacement mode shapes of the modes are given in Figure 17. The in plane bending modes are denoted with 'B', the lateral bending modes with 'L' and the torsion modes with 'T'.

Table 1: Material properties applied in the FEM.

Young's modulus (E_{cm})	Density (ρ_m)	Poisson's ratio (ν)
46 GPa	2350 Kg/m^3	0.2

4. Acceleration-based modal analysis

For this modal analysis, only the data obtained from the uniaxial accelerometers are used. Since the data are obtained from two different acquisition systems (one for the vertical and one for the lateral accelerometers) and are sampled with different sampling frequencies, two independent modal analyses are conducted. More specifically, the first modal analysis is conducted with the data from the accelerometers that are measuring in the vertical direction while the second with the data from the accelerometers that are measuring in the lateral direction.

The system identification is conducted with MACEC, a MatLab toolbox for experimental and operational modal analysis [33]. Two identification techniques are applied: covariance-driven Stochastic Subspace Identification (SSI-cov), which is an output only identification technique [34, 35, 36], and Combined deterministic-stochastic Subspace Identification (CSI) [37], where both the input force and the output measured data (accelerations, strains, etc.) are used for the identification. The SSI-cov algorithm provides also the 95% confidence intervals (CI=$[-2\sigma, 2\sigma]$) for quantifying the uncertainty of the identified dynamic characteristics. In both techniques, the maximum system order and the half number of Hankel's block rows i need to be defined [35, 37]. Their values are summarized in Table 2 for both techniques and both modal analyses. Since the CSI algorithm is a deterministic-stochastic algorithm, a higher accuracy can be obtained with a lower system order. Furthermore, the computational effort for the CSI algorithm is higher than for the SSI-cov algorithm, forcing the user to choose a lower system order with respect to the SSI-cov algorithm, without though compromising the identification accuracy. In both applied techniques,

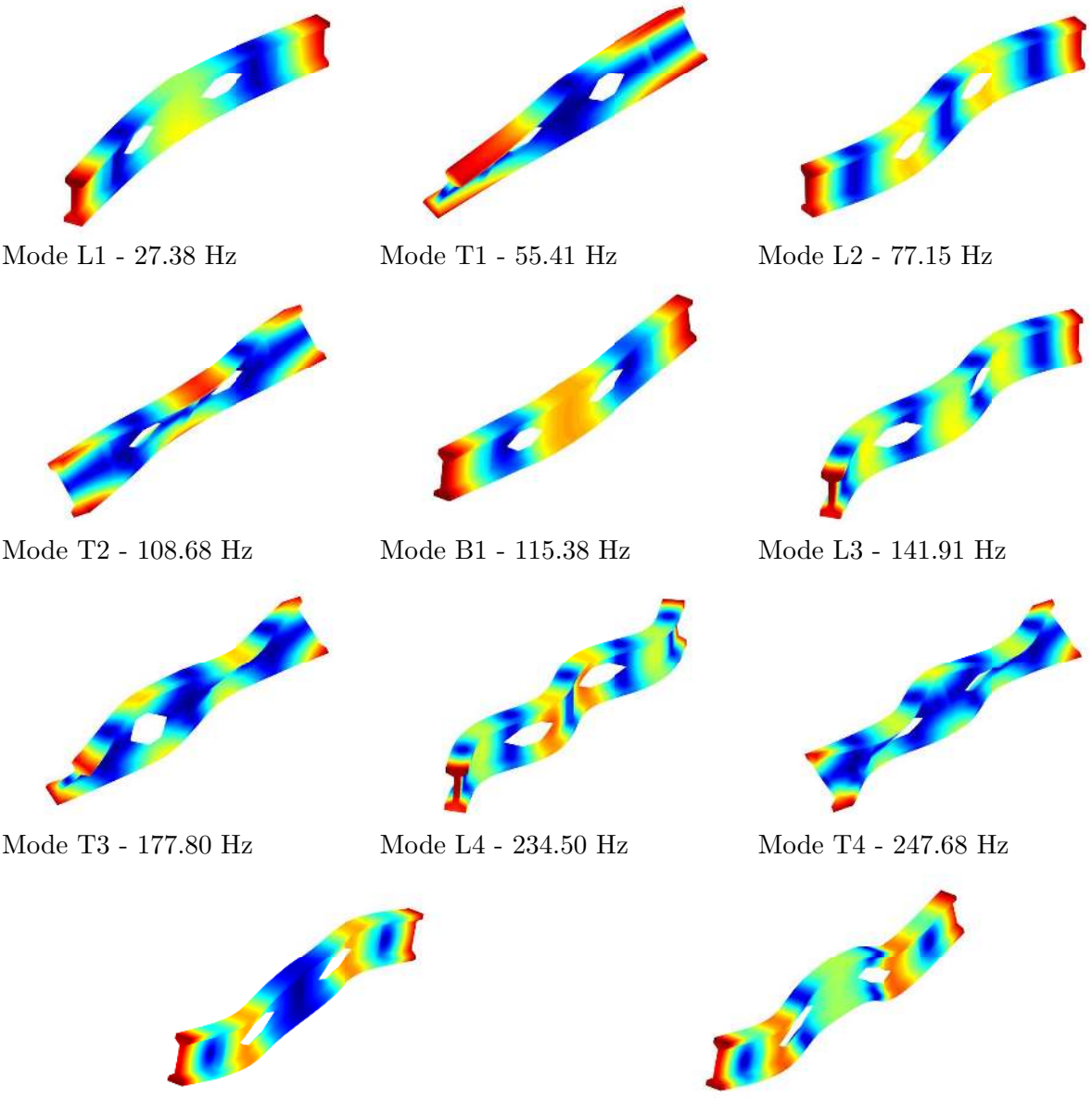

Figure 17: Mass-normalized displacement mode shapes, as calculated by the FEM. The total modal displacements of each mode are plotted.

the system identification is performed in the time domain. During data processing, the static or DC (Direct Current) offset is removed from all measured signals.

4.1. Natural frequencies

Eleven vertical, lateral, and torsion modes are identified in the frequency range [0-350] Hz and are manually selected from stabilization diagrams [38]. Obviously, the in plane bending modes are identified from the modal analysis using vertical accelerometer data while the lateral bending

Table 2: Selected parameters for SSI-cov and CSI, for the acceleration-based modal analysis.

Data used for the identification	Identification method	Hankel's block rows i	System order
Vertical accelerations	CSI	50	2:2:80
Vertical accelerations	SSI-cov	50	2:2:100
Horizontal accelerations	CSI	60	2:2:70
Horizontal accelerations	SSI-cov	60	2:2:100

modes are identified from the modal analysis using horizontal accelerometer data. The torsion modes are identified from both modal analyses. The differences in natural frequencies between the two modal analyses for the commonly identified torsion modes are negligible ($\ll 1\%$). Therefore, for simplicity, the results of both modal analyses are presented together. The identified natural frequencies for both identification techniques and for the undamaged beam are presented in Table 3. The calculated 95% confidence interval ($\mathrm{CI_{f,a}}$) of the natural frequencies, which represents the variance error of the output-only identification with SSI-cov [36], is also provided. Furthermore, the natural frequencies of the numerical model are given for comparison purposes.

The differences in the natural frequency values between the SSI-cov and the CSI are minor and less than 1.0%. Moreover, the 95% confidence interval ($\mathrm{CI_{f,a}}$) is in all cases smaller than 0.52 Hz, indicating a high identification accuracy. When the experimentally identified and the numerically obtained natural frequencies are compared, a good match is observed for the lateral bending modes L1 and L2, the torsion modes T3 and T4 and the in plane bending modes B2 and B3. On the contrary, for the remaining modes a significant difference in the natural frequency values is observed. This is attributed to the interaction of the "roof" beam with the supporting beam, which is not taken into account by the FEM. In order to investigate which modes are influenced by the "roof" beam-supporting beam interaction, the Modal Assurance Criterion (MAC) [39], as a measure of consistency (degree of linearity) between the estimates of the modal vectors that are identified under different conditions is applied. The MAC can take values between zero (no consistency between the mode shapes) and unity (the mode shapes are consistent). Therefore, the MAC is applied between the calculated and the experimentally obtained displacement mode shapes of the undamaged beam. The MAC values are given in Figure 18. Two different MAC matrices are provided, as the in plane bending and torsion modes are obtained from the sensors on the top of the beam (Figure 10) while the lateral modes from the sensors on the side of the beam (Figure 12) and a direct comparison of them would not be valid. The MAC values for the first two lateral modes, L1 and L2 and the last two in plane bending modes B2 and B3 are approximating unity (> 0.98), indicating a high consistency between the calculated and the experimentally obtained modes. Therefore, for these modes the assumption of free-free boundary condition applies and the system "roof" beam-supporting beam is decoupled. Hence, it is expected that any potential changes on the dynamic characteristics of these modes will originate from the damage that is induced to the "roof" beam. Overall, it can be concluded that the natural frequencies are well identified from the experimental acceleration data while the FEM correctly estimates the natural frequencies and the displacement mode shapes of the decoupled modes.

Furthermore, the evolution of the natural frequencies throughout the PDT is shown in Figure 19. The presented natural frequencies correspond to the decoupled modes, namely modes L1, L2, B2 and B3. For the damage sensitive modes, a constant reduction of their natural frequency values is observed, which is correlated with the increased level of damage of the beam. The percentile

Table 3: Natural frequencies of the undamaged beam as obtained from SSI-cov ($f_{SSI,a}$) and CSI ($f_{CSI,a}$) identification for acceleration-based modal analysis. The 95% confidence interval ($CI_{f,a} = [-2\sigma_{f,a}, 2\sigma_{f,a}]$) as obtained from the SSI-cov is provided. The FEM natural frequenies (f_{FEM}) are also given.

Mode	Type	$f_{SSI,a} \pm 2\sigma_{f,a}$ [Hz]	f_{CSI} [Hz]	f_{FEM} [Hz]
1	L1	27.25±0.02	27.21	27.38
2	T1	34.05±0.03	33.88	55.41
3	L2	75.32±0.01	75.31	77.15
4	T2	92.85±0.08	92.36	108.68
5	B1	127.20±0.06	126.83	115.38
6	L3	128.72±0.20	129.22	141.91
7	T3	178.02±0.03	178.04	177.80
8	L4	216.50±0.03	216.62	234.50
9	T4	244.38±0.26	243.75	247.68
10	B2	265.92±0.03	265.97	264.40
11	B3	313.98±0.04	313.91	314.38

reduction of the natural frequency values varies form 4% to 9% for the different modes, depending on the degree that each mode is influenced by the damage. The natural frequency values as identified with the SSI-cov and the CSI are almost matching for all loading cycles, while the obtained 95% $CI_{f,a}$ from the SSI-cov is also relatively narrow. Therefore, the identification can be considered as highly accurate.

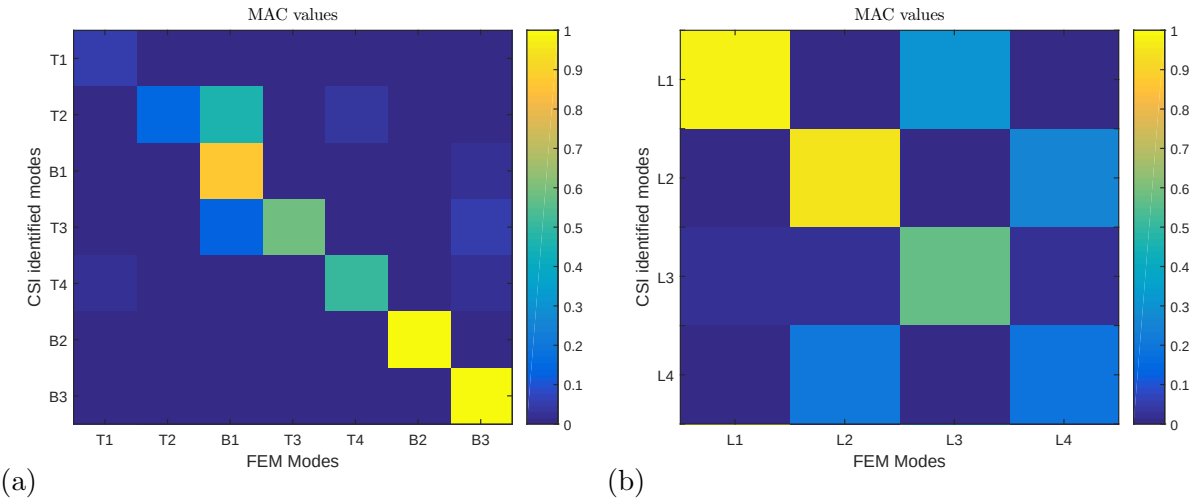

(a) (b)

Figure 18: MAC values between the displacement mode shapes (CSI) of the undamaged beam and the displacement mode shapes of the FEM. (a) MAC values for the in plane bending and torsion modes (b) MAC values for the lateral modes.

4.2. Displacement mode shapes

The influence of the damage on the displacement mode shapes of the identified decoupled modes is examined. Potential changes in the amplitude and curvature of the mode shapes would indicate the presence of damage at the vicinity of these zones. To demonstrate the evolution of the mode shapes throughout the PDT, combined graphs with the mode shapes that are identified in each

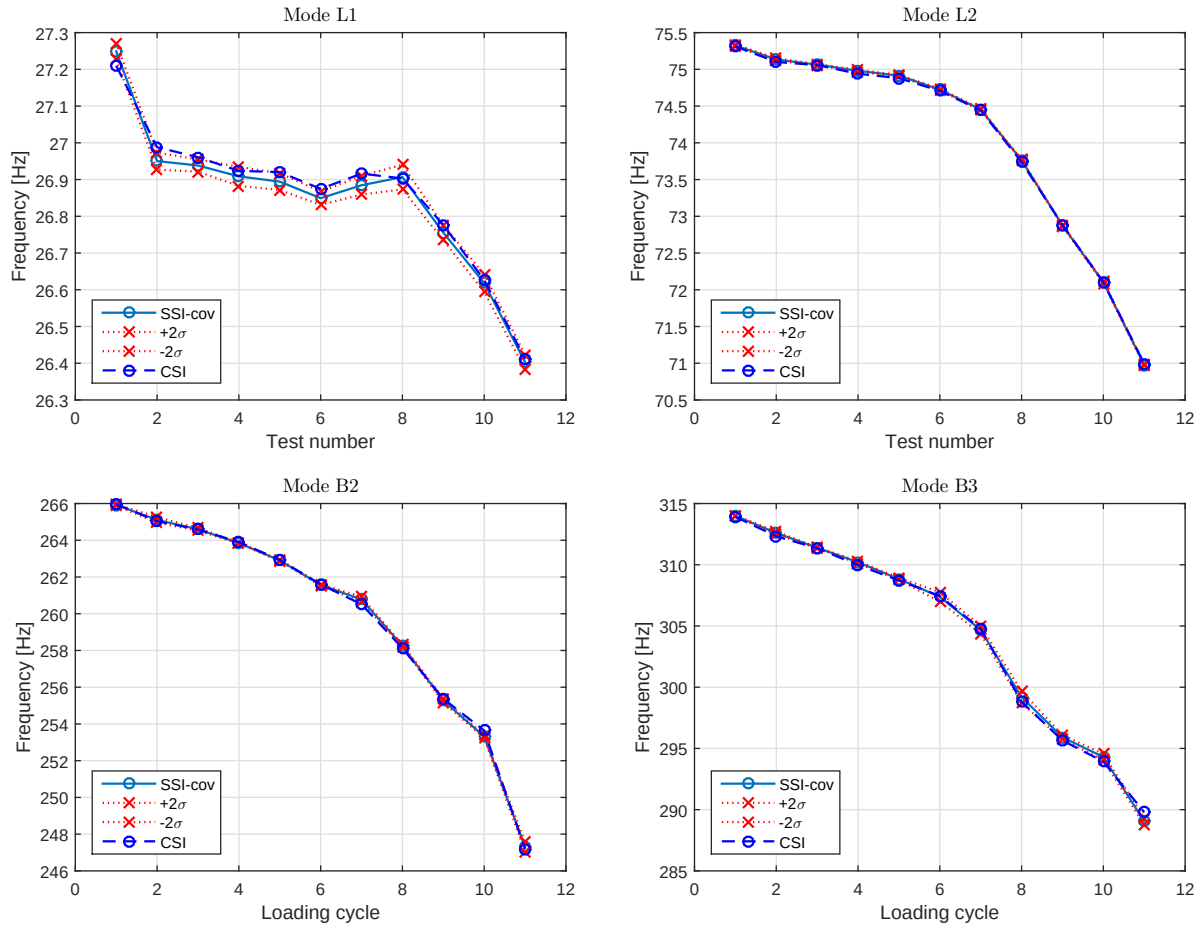

Figure 19: Evolution of the natural frequencies as identified from the acceleration data, using SSI-cov (continuous lines) and CSI (dashed lines). For SSI-cov, the 95% confidence intervals are also available (dotted lines).

loading cycle are presented. A least-squares fit is applied for the determination of the scale factor c that links the mode shapes of the various cycles with the mode shapes of the undamaged beam. The displacement mode shapes (CSI) of the decoupled modes (L1, L2, B2 and B3) are shown in Figure 20.

The lateral modes are obtained from the accelerometers that are recording the lateral response of the beam (Figure 12). Since only one row of sensors is used, the mode shapes are represented by a single curve (Figures 20a and 20b). The sensor in location L6 was damaged during the experiment and therefore its data are neglected during the modal analysis. Thus, the L2 mode shape appears to be flat at the location where sensor L6 is (x=4200 mm). The in plane bending modes are obtained from the accelerometers on the top of the beam (Figure 10). Since two rows of sensors are used, the mode shapes can be described with two curves. In Figures 20c and 20d, the top subplots correspond to the side of the beam with positive y-coordinate and the bottom to the side of the beam with negative y-coordinate (Figure 10).

The displacement mode shapes of the presented modes (Figure 20) do not appear to be substantially influenced by the increased level of damage in the beam. More specifically, no significant amplitude or curvature changes are observed that would indicate the detection of damage. Fur-

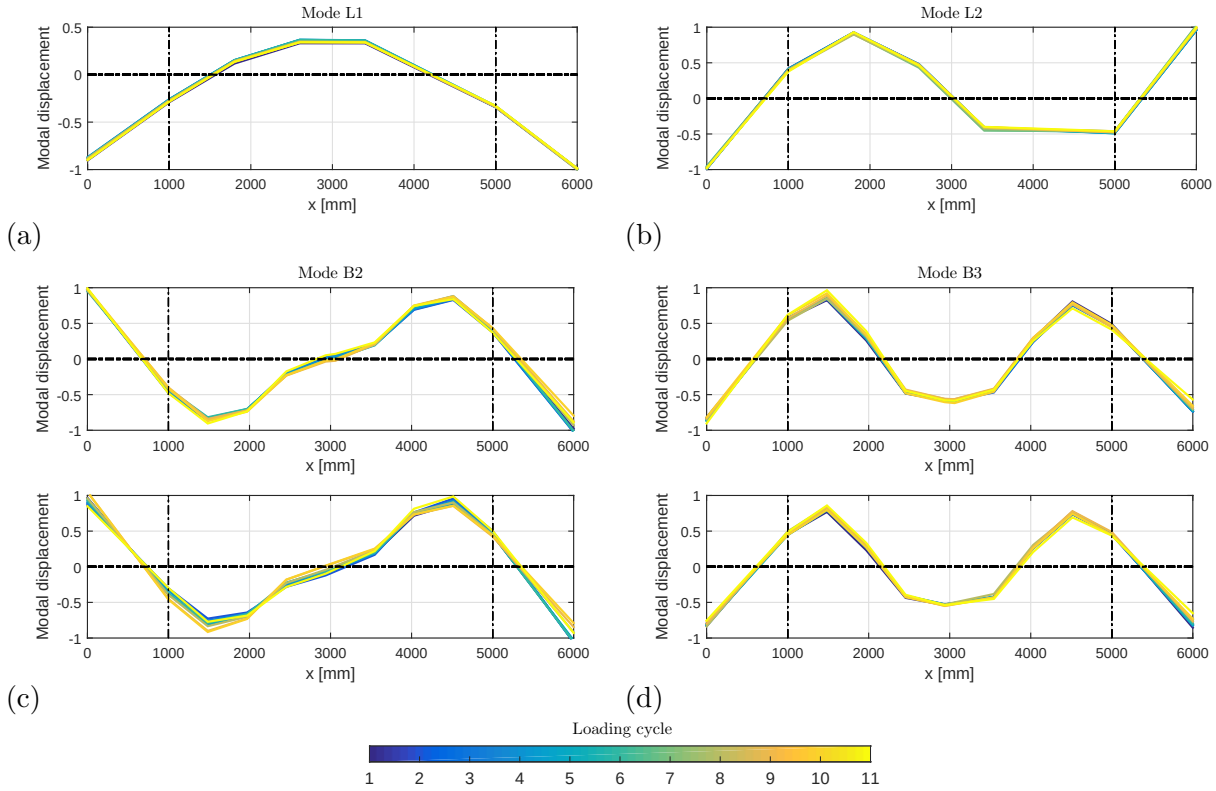

Figure 20: Evolution of the displacement mode shapes as identified from CSI, for the 11 loading cycles. In (c) and (d), the top subplots correspond to the side of the beam with positive y-coordinate and the bottom to the side of the beam with negative y-coordinate. The dash-dotted lines indicate the location of the supports. (a) Mode L1, (b) Mode L2, (c) Mode B2, and (d) Mode B3.

thermore, the MAC is applied to identify any potential changes on the displacement mode shapes that are not identified by their visual inspection. The displacement mode shapes of the undamaged beam are considered as the base mode shapes, and are compared with the mode shapes of the different damaged states. The MAC values of the mode shapes for the different damage levels are compared in Figure 21. The MAC values approximate unity (> 0.97) for all modes throughout the PDT, indicating insignificant changes of the mode shapes and what is observed in Figure 20; the damage is not identified by the displacement mode shapes.

5. Strain-based modal analysis

Dynamic strain data, obtained from the FBG strain sensors are used for the second modal analysis. The average measured root mean square (RMS) strain values among all FBGs are $\approx 0.35\mu\epsilon$ for the vertical impact tests and $\approx 0.15\mu\epsilon$ for the lateral impact tests, similar to the values occurring on civil structures during ambient or operational excitation. The dynamic input force cannot be sampled with the FBG interrogator since the hammer that is used for the excitation of the beam has a piezoelectric force sensor. Therefore, only the measured dynamic strains are used in the system identification resulting in an output-only modal analysis. The system identification is performed with the SSI-cov technique. The model order is chosen in steps of 2 and the maximum

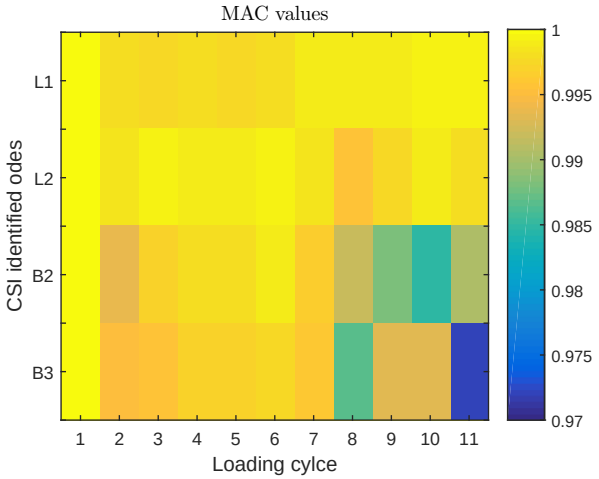

Figure 21: MAC values between the undamaged displacement mode shapes and the displacement mode shapes of the various damage levels for modes L1, L2, B2 and B3.

order is 120. The half number of Hankel's block rows i is 50. During data processing, the static or DC offset is removed from all measured signals. Furthermore, a 4^{th} order Butterworth filter with a high-pass frequency of 2 Hz is applied to all channels to remove the influence of the small temperature fluctuations during the PDT on the strain measurements.

5.1. FBG synchronization

The tunable laser FBG interrogator does not simultaneously scan the various FBG sensors but instead makes a high-speed sweep scan of about 0.1 pm/ns along its wavelength bandwidth, achieving in this way high wavelength resolution. However, due to the sweep, a delay is introduced in the measurements which leads to a phase shift between the FBGs. As a solution, a novel offline synchronization technique [26] is applied to synchronize the FBGs. The technique makes use of the identified modal strains to calculate the time delay between the various FBGs and consequently corrects the modal strains. The technique assumes linear dynamic behavior of the structure and proportional damping of the structural modes.

The time delay δt^* can be estimated by minimization of the objective function $f(\delta t)$ (Equation 1) that gives the average difference between the mean phases (MP) [38] of the complex modal strains, $\Phi_{com,m}$, and the reference modal strain, $\Phi_{ref,m}$, over all modes (n_m) [26]. The complex modal strains are defined here as the modal strains that need to be corrected (the modal strains obtained from the FBG sensors that are interrogated with a time delay due to the linear sweep) with respect to the reference modal strain (the modal strain obtained from the FBG sensor which is interrogated first).

$$\delta t^* = \text{argmin} f(\delta t) = \text{argmin} \frac{1}{n_m} \sum_{m=1}^{n_m} |\text{MP}(\Phi_{com,m} e^{\lambda_{m1} \delta t}) - \text{MP}(\Phi_{ref,m})| \tag{1}$$

The rescaling of the complex modal strains is obtained by multiplying them by a factor A_m (Equation 2) which is defined as [26]:

$$A_m = e^{\lambda_{m1} \delta t^*} \tag{2}$$

where $\lambda_{m1} = -\omega_m \xi_m + i\omega_m \sqrt{1-\xi_m^2}$ is the pole correspond to the natural frequency ω_m and modal damping ratio ξ_m of mode m. An experimental modal analysis on a steel I-beam was performed [40], where the implementation of the offline synchronization technique on the strain mode shapes as obtained from the FAZT data is analytically described. The reader is referred to [26, 40] for further details.

5.2. Natural frequencies

Eleven modes, the same as in the acceleration-based modal analysis, are identified. The in plane bending modes are identified from the tests where the excitation is in the vertical direction of the beam (z-axis in Figure 14) while the lateral bending modes from the tests where the excitation is in the lateral direction of the beam (y-axis in Figure 14). The torsion modes are identified from both tests. Therefore, the results of modal analyses of the vertical and the lateral tests are presented together. The identified natural frequencies for the undamaged beam are presented in Table 4. The calculated 95% confidence interval ($CI_{f,s}$) of the natural frequencies is also provided. Furthermore, the identified natural frequencies of the acceleration-based modal analysis are given for comparison purposes.

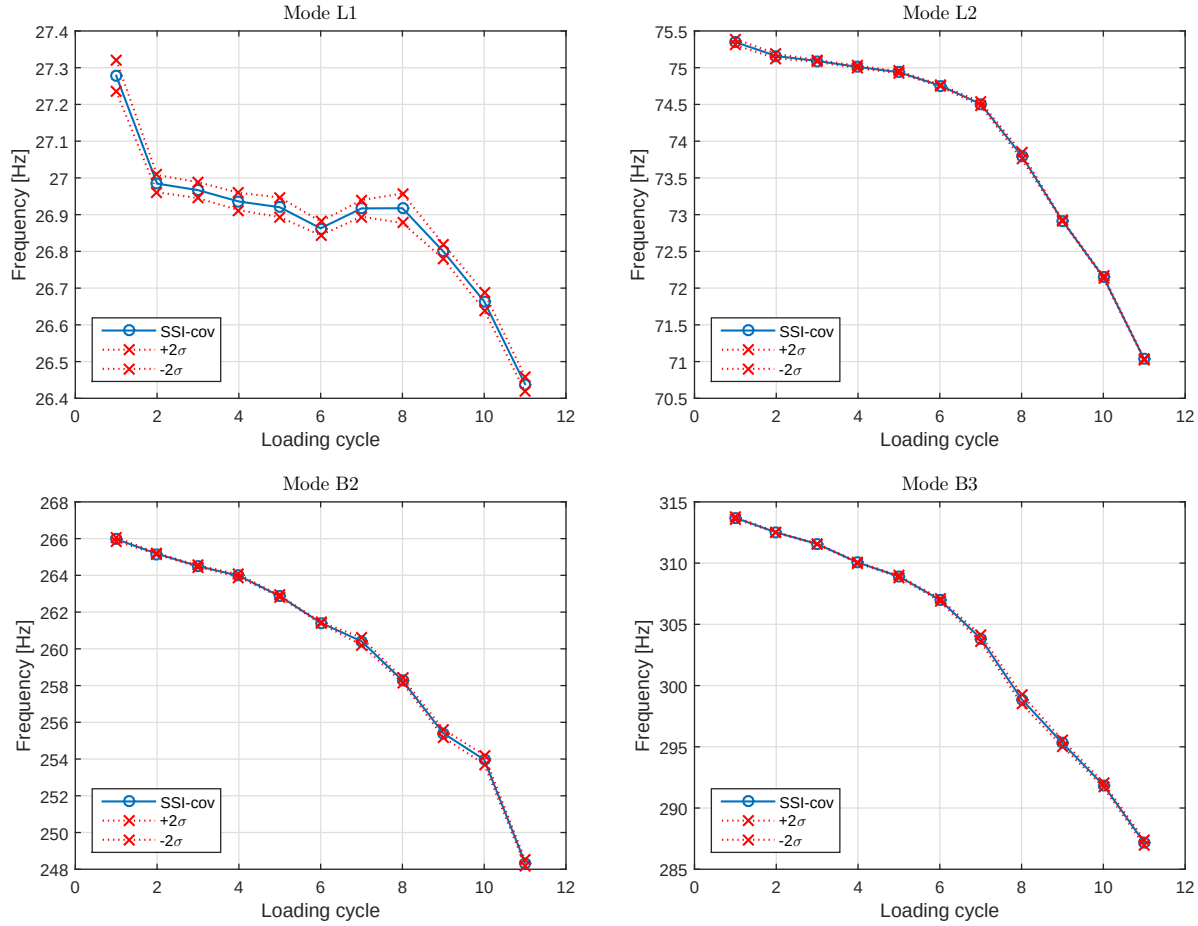

Figure 22: Evolution of the natural frequencies as identified from the FBG strain data (solid lines) and their 95% confidence intervals (dotted lines).

Table 4: Natural frequencies of the undamaged beam as obtained from SSI-cov ($f_{SSI,s}$) identification for the FBG data modal analysis. The 95% confidence interval ($CI_{f,s} = [-2\sigma_f, 2\sigma_f]$) as obtained from the SSI-cov, is also provided. The natural frequenies ($f_{SSI,a}$) as obtained from the acceleration-based modal analysis with their 95% ($(CI_{f,a})$ confidence interval are also given.

Mode	Type	$f_{SSI,s} \pm 2\sigma_{f,s}$ [Hz]	$f_{SSI,a} \pm 2\sigma_{f,a}$ [Hz]
1	L1	27.28±0.04	27.25±0.02
2	T1	35.21±0.04	34.05±0.03
3	L2	75.35±0.04	75.32±0.01
4	T2	92.94±0.18	92.85±0.08
5	B1	126.96±0.06	127.20±0.06
6	L3	129.45±0.03	128.72±0.20
7	T3	178.02±0.04	178.02±0.03
8	L4	216.58±0.04	216.50±0.03
9	T4	244.37±0.13	244.38±0.26
10	B2	265.97±0.09	265.92±0.03
11	B3	313.70±0.08	313.98±0.04

The differences in the identified natural frequency values between the acceleration-based and the strain-based modal analyses are less than 1.0%. Moreover, the 95% confidence interval ($CI_{f,s}$) is in all cases smaller than 0.36 Hz, indicating a high identification accuracy. Obviously, since the natural frequencies obtained from the strain data are almost matching with the ones obtained from the accelerometer data, the same conclusions regarding their relationship with the calculated values are drawn. Therefore, a good match is observed for the modes that are not influenced by the supporting beam-"roof" beam interaction (L1, L2, B2 and B3).

Furthermore, the evolution of the natural frequency values throughout the PDT is given in Figure 22. The percentile reduction of the natural frequency values varies form 4% to 9% for the different modes, depending on the degree that each mode is influenced by the damage. The identified natural frequency values at each damaged state are matching with the values obtained from the accelerometer data. Moreover, the obtained 95% $CI_{f,s}$ from the SSI-cov is also relatively narrow for all loading cycles. Therefore, the identification can be considered as highly accurate.

5.3. Strain mode shapes

In this section, the influence of the increasing damage throughout the PDT on the strain mode shapes is investigated. Combined graphs are given, where the identified strain mode shapes of a mode in each loading cycle are plotted on top of each other. A least-squares fit is applied for the determination of the scale factor c that links the strain mode shapes of the various loading cycles with the strain mode shapes of the undamaged beam. The least-squares fit is calculated to the modal strain values at the ends of the fibers i.e., the zones outside of the static supports. Since these zones are not stressed due to the static loading, their values are not expected to change due to the imposed damage. The mode shapes of modes L1, L2, B2 and B3 are shown in Figure 23. The top subplots correspond to the top flange fibers while the bottom to the bottom flange fiber (Figure 14). The experimentally obtained strain mode shapes are corrected for the phase shift that is introduced by the high-speed sweep of the FBG interrogator. The corrected mode shapes exhibit close to unity modal phase collinearity (MPC) [41] values. This is an indication of non-complex, almost purely real modes.

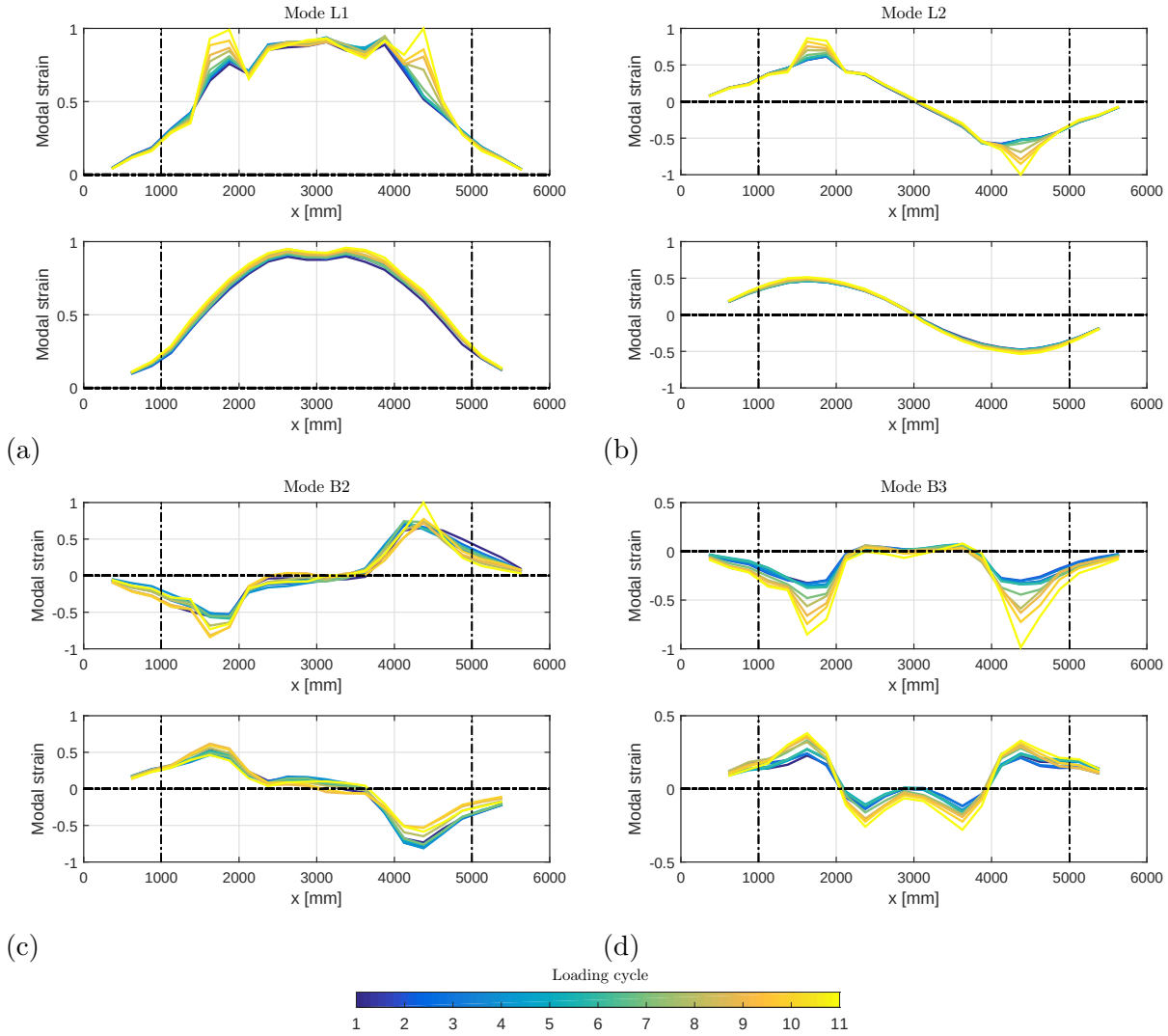

Figure 23: Evolution of the damage sensitive strain mode shapes as identified from SSI-cov, for the 11 loading cycles. The top subplots correspond to the top flange fibers of the beam while the bottom to the bottom flange fiber. The dash-dotted lines indicate the location of the supports. (a) Mode L1, (b) Mode L2, (c) Mode B2, and (d) Mode B3.

Significant amplitude changes are observed in the vicinity of the damaged area (around the openings of the web), as can be seen from the strain mode shapes in Figure 23. The increase in amplitude is directly related to the decrease of stiffness at certain locations of the beam (x≈1500 mm and x≈4500 mm) where shear cracks were observed during the experiment (Figure 6). The strain mode shapes are mainly influenced by cracks 8-11, which increase in size throughout the PDT, as shown in Figure 7. The evolution of the strain mode shapes during the different loading cycles is prominent and follows the evolution of the cracks. The highest modal strain amplitude values at the location of the damage (Figure 23) correspond to the last loading cycle, where the beam is heavily damaged and close to failure. The top flange strain mode shapes appear to be more sensitive to damage, which is in agreement with the observations during the experiment where the most severe cracks were observed at the top of the beam. However, both the top and the bottom

strain mode shape of mode B3 (Figure 23d) are influenced from the damage, allowing in this way to identify also damage of moderate severity at the bottom flange of the beam. The distribution of the damage in the beam, explains also why the natural frequencies of modes L1, L2, B2 and B3 are highly influenced. At the vicinity of the damaged zones, the changes of the strain mode shapes are high and as a result the reduction of stiffness at these areas affects the natural frequencies.

In contrast with the displacement mode shapes, the strain mode shapes are heavily influenced from the damage. This influence becomes apparent from the sixth loading cycle on mode B3 and the seventh loading cycle for the other modes. In these loading cycles, the observed crack lengths and widths are still small: the measured crack width after the end of these loading cycles was only about 25% of the final crack width that was measured after the end of the last loading cycle at 500 kN.

The MAC is applied between the identified strain mode shapes of the undamaged beam and the numerically obtained strain mode shapes from the FEM (Figure 24). The MAC values of the main diagonal approximate unity (> 0.93), supporting the assumption that modes L1, L2, B2 and B3 are dynamically decoupled and exhibit dynamic free-free boundary conditions. Furthermore, the MAC is applied between the strain mode shapes of the different damage levels (Figure 25). The strain mode shapes of the undamaged beam are considered as the base mode shapes. The MAC values are approximating unity (> 0.95) for modes L1 and L2 throughout the PDT, exhibiting a low damage sensitivity. However, for modes B2 and B3, MAC values decrease in correlation with the increased damage of the beam and take values as low as 0.87, indicating higher sensitivity as a damage indicator. The difference is attributed to the influence that the damage has on each mode shape. For modes B2 and B3, the shear damage of the beam influences both the top and the bottom flange mode shapes. Thus, the MAC values drop more for these modes than for the others where the bottom flange mode shapes appear to be uninfluenced. Furthermore, damage has a more generic influence on the strain mode shapes of modes B2 and B3 in comparison with the mode shapes of modes L1 and L2, where changes in amplitude and curvature are observed in discrete locations. This further contributes to the lower MAC values of modes B2 and B3.

Finally, a quantity for damage detection and localization is introduced: the top-to-bottom strain ratio (TBSR), which is defined as:

$$TBSR(x) = \frac{|\epsilon_{top}(x)|}{|\epsilon_{bottom}(x)|} \tag{3}$$

where $|\epsilon_{top}(x)|$ is the absolute value of the longitudinal modal strain at the top of the beam, $|\epsilon_{bottom}(x)|$ is the absolute value of the longitudinal modal strain at the bottom of the beam, and x denotes, as before, the longitudinal coordinate. The TBSR is computed for the well-identified strain mode shapes of the in plane bending modes, B2 and B3. At the locations that the modal strains are approximating zero, mainly in the zone between 2700-3300 mm, the criterion is not applied since the division by very small quantities can yield inaccurate results. As can be clearly seen in Figure 26, where the evolution of the TBSR values along the beam for modes B2 and B3 throughout the PDT are given, the influence of the damage is significant. A clear increase or decrease of the TBSR at the locations where the damaged was mainly observed during the PDT (Figure 6), indicates its high sensitivity as a damage indicator. These changes appear already from the second loading cycle and become really apparent after the sixth loading cycle. The largest changes are observed at the zones around 1500 mm and 4500 mm, where the most severe cracks were observed during the PDT (Figure 26c). There, the TBSR values have a percentile increase

of up to 114% between the undamaged beam and the damaged beam of the last loading cycle. Therefore, the TBSR is considered as a high sensitivity measure of the level of damage.

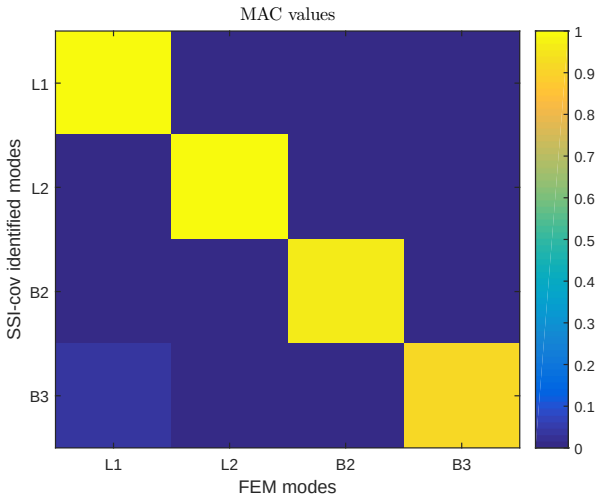

Figure 24: MAC values between the undamaged beam strain mode shapes (SSI-cov) and the numerical strain mode shapes for modes L1, L2, B2 and B3.

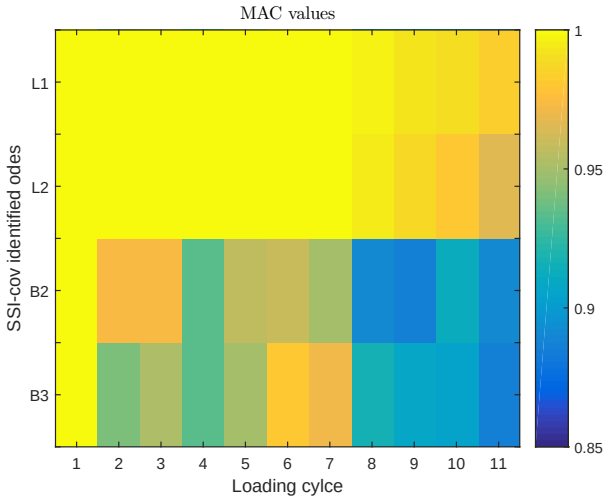

Figure 25: MAC values between the undamaged beam strain mode shapes and the strain mode shapes of the various damage levels for modes L1, L2, B2 and B3.

It may be noted that, for bending cracks in solid beams, the TBSR is directly related to the local shift of the neutral axis induced by the bending cracks. While the present beam has a more complex structural behavior and a different cracking pattern, the TBSR still appears to provide useful information regarding the presence and location of the cracks. Further post-processing of modal strains (or modal curvatures) would be directly useful for damage identification methods based on modal curvatures, modal strains or modal energies. [11, 42, 43, 44, 45].

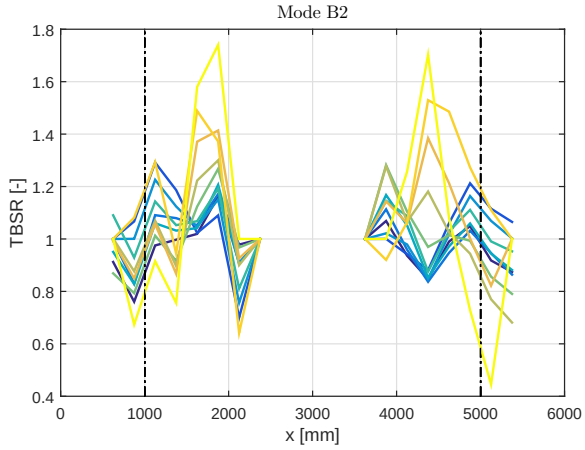

(a)

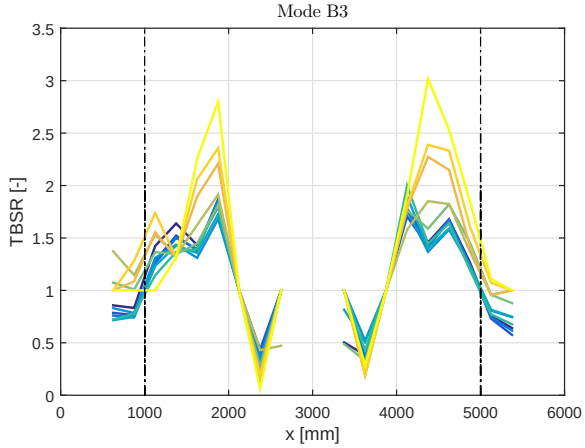

(b)

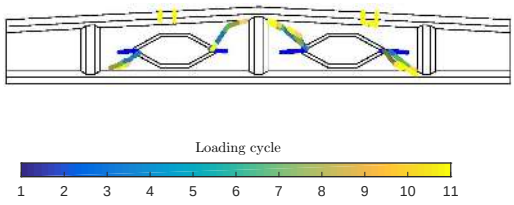

(c)

Figure 26: TBSR values between the undamaged beam strain mode shapes and the strain mode shapes of the various damage levels. The black dashed lines indicate the location of the supports. (a) Mode B2, (b) Mode B3. The pattern of the main cracks is also provided in (c).

6. Conclusions

In this paper, a new method was presented for vibration-based structural health monitoring by means of quasi-distributed longitudinal macro-strain FBG sensing. The method was demonstrated and validated by progressive damage testing of a "roof" beam displaying more complex structural behavior than regular beam-type structures.

While the dynamic strain amplitudes were very low (sub-microstrain RMS values were observed), the experimentally identified natural frequencies and strain mode shapes were seen to be very accurate. This indicates that the proposed combination of a high-accuracy tunable laser FBG interrogator, advanced parametric system identification techniques, and an offline compensation of the delays introduced by the interrogator, will be adequate also for large-scale civil structures.

The damage that was induced into the "roof" beam by the progressive damage test caused important changes in the natural frequencies and strain mode shapes identified from the FBG data in a relatively early stage, while the displacement mode shapes that were identified from conventional modal testing with accelerometers were insensitive even to very severe damage. This confirms that strain mode shapes are much more sensitive to local damage than displacement mode shapes, even in this rather complex case where most cracks do not appear away from the strain sensors. The sensitivity becomes even larger when the ratio between the modal strain amplitudes at the top and the bottom of the beam (termed TBSR or top-to-bottom strain ratio in this paper) are taken.

[1] Farrar CR and Worden K. *Structural Health Monitoring: A Machine Learning Perspective*. 1^{st} ed. West Sussex: John Willey & Sons, 2013.

[2] Magalhaes F, Cunha A and Caetano E. Dynamic monitoring of a long span arch bridge. *Engineering Structures* 2008; 30(11): 3034–3044.

[3] Brownjohn J, De Stefano A, Xu YL, Wenzel H and Aktan A. Vibration-based monitoring of civil infrastructure: challenges and successes. *Journal of Civil Structural Health Monitoring* 2011; 1(3–4): 79–95.

[4] Reynders E, Wursten G and De Roeck G. Output-only structural health monitoring in changing environmental conditions by means of nonlinear system identification. *Structural Health Monitoring* 2014; 13(1): 82–93.

[5] Deraemaeker A, Reynders E, De Roeck G and Kullaa J. Vibration based Structural Health Monitoring using output-only measurements under changing environment. *Mechanical Systems and Signal Processing* 2008; 22(1): 34–56.

[6] Peeters B and De Roeck G. One-year monitoring of the Z24-bridge: environmental effects versus damage events. *Earthquake Engineering and Structural Dynamics* 2001; 30(2): 149–171.

[7] Ni YQ, Hua XG, Fan KQ and Ko JM. Correlating modal parameters with temperature using long-term monitoring data and support vector machine technique. *Engineering Structures* 2005; 27(12): 1762–1773.

[8] Saisi A, Gentile C and Guidobaldi M. Post-earthquake continuous dynamic monitoring of the Gabbia Tower in Mantua, Italy. *Construction and Building Materials* 2015; 81: 101–112.

[9] Gentile C, Guidobaldi M and Saisi A. One-year dynamic monitoring of a historic tower: damage detection under changing environment. *Meccanica* 2016; 51(11): 2873–2889.

[10] Cavalagli N, Comanducci G and Ubertini F. Earthquake-induced damage detection in a monumental masonry bell-tower using long-term dynamic monitoring data. *Journal of Earthquake Engineering* 2017.

[11] Pandey AK, Biswas M and Samman MM. Damage detection from changes in curvature mode shapes. *Journal of Sound and Vibration* 1991; 145(2): 321–332.

[12] Reynders E, De Roeck G, Bakir P and Sauvage C. Damage identification on the Tilff bridge by vibration monitoring using optical fibre strain sensors. *ASCE Journal of Engineering Mechanics* 2007; 133(2): 185–193.

[13] Unger J, Teughels A and De Roeck G. Damage detection of a prestressed concrete beam using modal strains. *ASCE Journal of Structural Engineering* 2005; 131(9): 1456–1463.

[14] Adewuyi AP, Wu ZS and Serker NHMK. Assessment of vibration-based damage identification methods using displacement and distributed strain measurements. *Structural Health Monitoring* 2009; 8(6): 443–461.

[15] Glišić B and Inaudi D. *Fibre optic methods for structural health monitoring*. Chichester, UK: John Wiley & Sons, 2007.

[16] Lee BH, Kim YH, Park KS, Eom JB, Kim MJ, Rho BS and Choi HY. Interferometric Fiber Optic Sensors. *Sensors* 2012; 12(3): 2467–2486.

[17] Liu K, Reynders E, De Roeck G and Lombaert G. Experimental and numerical analysis of a composite bridge for high speed trains. *Journal of Sound and Vibration* 2009; 320(1-2): 201–220.

[18] Glisic B and Inaudi D. Development of method for in-service crack detection based on distributed fiber optic sensors. *Structural Health Monitoring* 2012; 11(2): 161–171.

[19] Meltz G, Morey WW and Glenn WH. Formation of Bragg gratings in optical fibers by a transverse holographic method. *Optics Letters* 1989; 14(15): 823–825.

[20] Moyo P, Brownjohn JMW, Suresh R and Tjin SC. Development of Fiber Bragg grating sensors for monitoring civil infrastructure. *Engineering Structures* 2005; 27(12): 1828–1834.
[21] Roveri N, Carcaterra A and Sestieri A. Real-time monitoring of railway infrastructures using fibre Bragg grating sensors. *Mechanical Systems and Signal Processing* 2015; 60-61: 14–28.
[22] Arsenault TJ, Achuthan A, Marzocca P, Grappasonni C and Coppotelli G. Development of a FBG based distributed strain sensor system for wind turbine structural health monitoring. *Smart Materials and Structures* 2013; 22(7): 11.
[23] Rodrigues C, Flix C, Lage A and Figueiras J. Development of a long-term monitoring system based on FBG sensors applied to concrete bridges. *Engineering Structures* 2010; 32(8): 1993–2002.
[24] Chan THT, Yu L, Tam HY, Ni YQ, Liu SY, Chung WH and Cheng LK. Fiber bragg grating sensors for structural health monitoring of Tsing Ma bridge: background and experimental observation. *Engineering Structures* 2006; 28(5): 648–659.
[25] Anastasopoulos D, Moretti P, Geernaert T, De Pauw B, Nawrot U, De Roeck G, Berghmans F and Reynders E. Identification of modal strains using sub-microstrain FBG data and a novel wavelength-shift detection algorithm. *Mechanical Systems and Signal Processing* 2017; 86A: 58–74.
[26] Maes K, Reynders E, Rezayat A, De Roeck G and Lombaert G. Offline synchronization of data acquisition systems using system identification. *Journal of Sound and Vibration* 2016; 381: 264–272.
[27] European Committee for Standardization. *NBN EN 12390-3: Testing hardened concrete - Part 3: Compressive strength of test specimens*, 2009.
[28] European Committee for Standardization. *EN 14651: Test method for metallic fiber concrete - Measuring the flexural tensile strength (limit op proportionality (LOP) residual)*, 2014.
[29] European Committee for Standardization. *NBN EN 12390-13: Testing hardened concrete - Part 13: Testing hardened concrete - Part 13: Determination of secant modulus of elasticity in compression*, 2013.
[30] European Committee for Standardization. *NBN EN 12390-13: Testing hardened concrete - Part 1: Shape, dimensions and other requirements for specimens and moulds*, 2001.
[31] Taylor JR. *An Introduction to Error Analysis: The Study of Uncertainties in Physical Measurements*. 2nd ed. Sausalito, CA: University Science Books, 1997.
[32] ANSYS Inc. *Elements Reference, ANSYS Release 15.0*, 2013.
[33] Reynders E, Schevenels M and De Roeck G. MACEC 3.3: a Matlab toolbox for experimental and operational modal analysis. Report BWM-2014-06, Department of Civil Engineering, KU Leuven, 2014.
[34] Peeters B and De Roeck G. Reference-based stochastic subspace identification for output-only modal analysis. *Mechanical Systems and Signal Processing* 1999; 13(6): 855–878.
[35] Reynders E, Pintelon R and De Roeck G. Uncertainty bounds on modal parameters obtained from Stochastic Subspace Identification. *Mechanical Systems and Signal Processing* 2008; 22(4): 948–969.
[36] Reynders E, Maes K, Lombaert G and De Roeck G. Uncertainty quantification in operational modal analysis with stochastic subspace identification: validation and applications. *Mechanical Systems and Signal Processing* 2016; 66–67: 13–30.
[37] Reynders E and De Roeck G. Reference-based combined deterministic-stochastic subspace identification for experimental and operational modal analysis. *Mechanical Systems and Signal Processing* 2008; 22(3): 617–637.
[38] Reynders E, Houbrechts J and De Roeck G. Fully automated (operational) modal analysis. *Mechanical Systems and Signal Processing* 2012; 29: 228–250.
[39] Allemang RJ. The Modal Assurance Criterion – Twenty Years of Use and Abuse. *Sound and Vibration Magazine* 2003; : 14–21.
[40] Anastasopoulos D, Maes K, De Roeck G and Reynders E. A comparison of two data acquisition techniques for modal strain identification from sub-microstrain fbg data. Proceedings of the International Conference on Experimental Vibration Analysis for Civil Engineering Structures EVACES 2017, 12-14 July 2017, San Diego, CA, USA.
[41] Pappa RS, Elliott KB and Schenk A. Consistent-mode indicator for the eigensystem realization algorithm. *Journal of Guidance, Control and Dynamics* 1993; 16(5): 852–858.
[42] Maeck J, Abdel Wahab MM, Peeters B, De Roeck G, De Visscher J, De Wilde WP, Ndambi JM and Vantomme J. Damage identification in reinforced concrete structures by dynamic stiffness determination. *Engineering Structures* 2000; 22(10): 1339–1349.
[43] Fan W and Qiao P. Vibration-based Damage Identification Methods: A Review and Comparative Study. *Structural Health Monitoring* 2010; 10(1): 83–111.
[44] Ciambella J and Vestroni F. The use of modal curvatures for damage localization in beam-type structures. *Journal of Sound and Vibration* 2015; 340: 126–137.

[45] Wu S, Zhou J, Rui S, and Fei Q. Reformulation of elemental modal strain energy method based on strain modes for structural damage detection. *Advances in Structural Engineering* 2017; 20(6): 896–905.